

Highly reliable and large-scale simulations of promising argyrodite solid-state electrolytes using a machine-learned moment tensor potential

Ji Hoon Kim^a, Byeongsun Jun^b, Yong Jun Jang^b, Sun Ho Choi^b, Seong Hyeon Choi^b, Sung Man Cho^b, Yong-Gu Kim^b, Byung-Hyun Kim^c, Sang Uck Lee^{a,*}

^a School of Chemical Engineering, Sungkyunkwan University, Suwon 16419, Republic of Korea

^b Hyundai Motor Company, Hwasung-si, Gyeonggi-do 18280, Republic of Korea

^c Department of Applied Chemistry, Center of Bionano Intelligence Education and Research, Hanyang University, Ansan 15588, Republic of Korea



ARTICLE INFO

Keywords:

Solid-state electrolyte
Argyrodite
Grain boundary
Machine learning
Moment tensor potential
Simulation

ABSTRACT

The high ionic conductivity of argyrodite makes it an attractive candidate for solid-state electrolytes (SSEs) in all-solid-state Li-ion batteries (ASSBs). Although great effort has been devoted to using *ab initio* molecular dynamics (AIMD) to evaluate ionic conductivity and elucidate the Li-ion diffusion mechanism of argyrodite-based SSEs, limitations in system size, simulation temperatures, and time associated with AIMD make accurate predictions and analysis of Li-ion diffusion challenging. Here, we present a reliable, large-scale computational approach to realistic simulation of SSEs in the bulk and at the grain boundary (GB) based on moment tensor potentials (MTPs) trained at the van der Waals optB88 level of theory. MTPs enable sufficiently large-scale and long-time simulations that reflect all possible configurational disorder of experimental crystal structures and provide accurate ionic conductivities that are close to values measured experimentally in halogenated Li-argyrodite ($\text{Li}_6\text{PS}_5\text{X}$ [X = Cl, Br, I]). Our simulations show that the vibrational motion of a PS_4 polyhedron has a positive effect on ionic conductivity. We also developed an accurate MTP using an active-learning approach to exploring Li-ion diffusion at the GB in polycrystalline SSEs. Simulations of the molecular dynamics of large $\sum 5[100](021)$ (>10,000-atom) GB models reveal that Li-ion accumulation around the GB region retards ionic conductivity and extends into an interior region approximately 20 Å from the GB interface. This work provides a practical approach to realistic large-scale and interfacial GB simulations that are otherwise inaccessible through *ab initio* calculations by developing accurate machine-learned MTPs.

1. Introduction

Recently, much research and development effort has been devoted to expanding the practical application of Li-ion batteries (LIBs) beyond small electronic devices, such as mobile phones and tablets, to large electric vehicles. [1,2] However, LIBs that use existing organic liquid electrolytes are flammable and volatile, and suffer from low energy density, limiting their use in the transportation sector. [3] Therefore, all-solid-state Li-ion batteries (ASSBs) using solid-state electrolytes (SSEs) are attracting significant attention as the next-generation batteries due to their potential for improved stability and greater energy density. [4–6] Despite these advantages of SSEs, the greatest obstacle to the commercialization of SSEs in ASSBs is their low ionic conductivity (σ_{RT}) at room-temperature (RT) compared with liquid electrolytes. Considerable resources have been expended searching for SSEs with

high ionic conductivity. [7–13] Especially, sulfide-based SSEs such as $\text{Li}_{10}\text{GeP}_2\text{S}_{12}$ (LGPS) [14] and Li-argyrodite ($\text{Li}_{6-x}\text{PS}_{5-x}\text{X}_{1+x}$ [X = Cl, Br, I]) [15–23] have received considerable attention due to their σ_{RT} above 10 mS/cm, which is comparable to values typical of liquid electrolytes, and their simplicity of mechanical deformability. In addition, continuous efforts to improve the ionic conductivity and electrochemical and chemical stability of Li-argyrodite are being made by optimizing their composition. [24–28] However, the enormous number of compositions potentially available on the periodic table poses an irresistible challenge for researchers to find the best SSEs materials. Even though a computational tools of *ab initio* molecular dynamics (AIMD) based on the density functional theory (DFT) [29–31] can be used to evaluate σ_{RT} in SSE screening, [32–35] AIMD simulations are very expensive time-consuming calculations and often lead to large discrepancies between predicted and experimentally measured σ_{RT} values due to the

* Corresponding author.

E-mail address: suleechem@skku.edu (S.U. Lee).

high temperatures and short (approximately 100 ps) time scales of simulations for systems as small as around 10 Å.

An alternative simulation method for elucidating dynamics is molecular dynamics (MD), which can address the limitations of AIMD. Nevertheless, MD simulations cannot be initiated without a force field describing the potential energy of the system according to the types of atoms, bonds, and interactions between atoms (e.g., van der Waals forces and electrostatic interactions) that correspond to the structure and composition of the system of interest. A novel method is therefore needed to develop suitable force fields for the system of interest. Halogenated Li-argyrodite ($\text{Li}_6\text{PS}_5\text{X}$ (X=Cl, Br, I)) offers a unique property in that the ionic conductivity depends on the site disorder of single anions (S^{2-} and X⁻) at Wyckoff 4a and 4c sites. There are six possible site-disorder configurations, each of which has different structural stability and ionic conductivity. The bulk ionic conductivity must therefore be represented as a contribution of each configuration depending on the relative stability and ionic conductivity. The most thermodynamically stable configuration constitutes most of the argyrodite structure, contributing more to bulk ionic conductivity. In addition, the configuration with the lowest ionic conductivity would be expected to have a significant effect on bulk ionic conductivity, acting as a bottleneck to ion diffusion. Li-ion diffusion through the bulk argyrodite is limited by the slowest rather than the fastest diffusion region. Although we previously devised a method to evaluate bulk ionic conductivity by considering both the thermodynamic and kinetic effects,[36] this method requires very expensive and time-consuming AIMD calculations for each of the six configurations.

To overcome the disadvantages of MD and AIMD, a combination of the two methods using machine-learned potential has been proposed. [37] In this study, we describe a reasonable progress toward developing accurate and efficient moment tensor potentials (MTPs) using strategically constructed training sets. We performed MD simulations on halogenated Li-argyrodite ($\text{Li}_6\text{PS}_5\text{X}$ [X=Cl, Br, I]) systems for approximately 10 ns using MTPs trained at the van der Waals optB88 level of theory while considering the unavoidable site disorder of X⁻ and S²⁻ single anions in halogenated Li-argyrodite, which has been proven to be a major factor in Li-ion conductivity enhancement, by using $3 \times 3 \times 3$ supercell structure (>1000 s atoms) with six randomly arranged site-disorder configurations. In a single large-scale MD simulation of a random structure, we obtained a bulk σ_{RT} value of 2.3 mS/cm, which was in close agreement with an experimentally measured $\text{Li}_6\text{PS}_5\text{Cl}$ value. Additionally, we found that the vibrational motion of a PS₄ polyhedron is related to a high σ_{RT} in large-scale and long-time simulations of halogenated Li-argyrodite.

Taking advantage of large-scale MD simulations using an MTP, we analyzed the origin of the decrease in ionic conductivity at the grain boundary (GB). It is widely recognized that GBs in polycrystalline SSE can significantly reduce ionic conductivity, which is one of the most essential property of SSEs. However, the physical origin of the retardation effect caused by the GB remains unknown because the limited spatial resolution of modern experimental techniques[1] and the lack of GB characterization makes it difficult to experimentally analyze ionic conductivity at the atomic scale. Computational tools using DFT and AIMD are also difficult to apply to GB analysis due to limitations of large-scale simulation. We therefore developed an improved MTP using an active-learning approach to explore Li-ion diffusion in the GB region of polycrystalline SSEs and successfully interpreted the GB-induced retardation of ionic conductivity. Our results indicate that the machine-learned MTPs can provide practical approach for realistic large-scale and long-time simulations such as random supercell structures and interfacial GBs.

2. Computational details

All density functional theory (DFT) calculations and MD simulations were performed with the Vienna *ab initio* simulation package (VASP)

5.4.4) [38–41] and a large-scale atomic/molecular massively parallel Simulator (LAMMPS) [42] package, respectively. The processes involved in machine-learned MTP development [37,43] are illustrated in Fig. 1 with six steps including training set generation of all possible potential energy surfaces in the configuration space, MTP training based on DFT energies, and MD simulations for ionic conductivities. Snapshot extractions were performed with pymatgen, [44] and MTP training was performed by MLIP [45,46] and a materials machine learning (MAML) [47] python package. Input structure generation, visualization and trajectory analysis of LAMMPS were performed in OVITO. [48] All computational task management was supported by CCpy (<https://github.com/91bsjun/CCpy>).

2.1. Six characteristic site disorder configurations

Structural optimization of six characteristic site-disorder configurations was conducted using the projector augmented wave(PAW) [49,50] method and the Perdew–Burke–Ernzerhof (PBE) generalized gradient approximation (GGA) [51] functional. Structural information for the six characteristic site-disorder configurations in argyrodite is described in our previous work [36] and Figure S1 in Supplementary information. We used a Monkhost $2 \times 2 \times 2$ k-point mesh in each primitive lattice vector of the reciprocal space and a plane-wave cutoff of 500 eV.[52] Lattice constants and internal atomic positions were fully optimized until the residual forces were less than 0.04 eV/Å. Fig. 1(b) shows how large a given structure can cover a potential energy surface in arbitrary coordinate space. It is not possible to train an MTP for any arbitrary coordinate space using only six thermodynamically stable site-disorder configurations. Gray regions indicate the untrained regions that need to be covered by creating a new training set.

2.2. Generation of training sets by lattice strain

A reasonable way to generate additional training sets is to expand the region trained in step (1). We generated strained structures in all lattice directions with $\pm 5\%$ strain using the structures optimized in step (1) to ensure diversity. Although the untrained region shrunk slightly, the region was still too vast, and the generated structures were limited around the six thermodynamically stable structures. Therefore, it is necessary to drastically expand the trained area in coordinate space.

2.3. Generation of additional training sets with short-time AIMD simulations at high temperatures

To consider most structural configurations in coordinate space, we generated an amorphous structure with AIMD simulations using an NVT Nose-Hoover thermostat [53,54] for each characteristic site-disorder configuration at four temperatures, from 300 K to 1200 K at 300 K intervals, including above the melting temperature interval during 10 ps with a 2 fs timestep. A total of 12 NVT simulations were performed at three strained structures and four different temperatures for each characteristic site disorder configuration, and a total of 1200 snapshots (100 from each NVT simulation trajectory) were extracted. As halogenated Li-argyrodite has six site disorder configurations, a total of 7200 snapshot structures can be used as a training set to cover most untrained regions.

2.4. Energy and force calculation of training sets with different functionals

We made single-point DFT calculations to obtain the energy and force for 7200 snapshot structures. We then compared three DFT functionals—PBE, PBE-D3(BJ), [55] and optB88-vdw [56] — using the options from step (1) to determine which DFT functional generates more accurate MTP potentials. The calculated results for crystal structures, energy, and force were then applied to the following training sets.

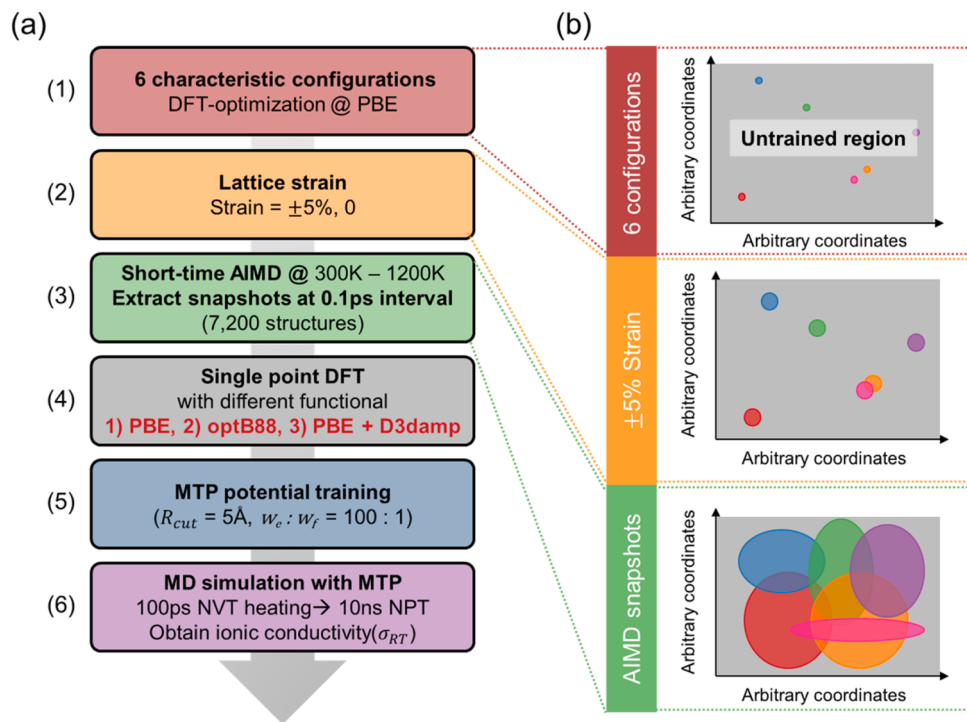


Fig. 1. (a) Machine-learned moment tensor potential (MTP) development workflow. (b) A schematic diagram of trained and untrained regions in an arbitrary coordinate space according to training sets. The gray region and colored circle represent untrained and trained regions, respectively.

2.5. MTP training according to each DFT functional

Recently, various machine-learning potentials, such as neural network potential (NNP), [57] deep potential (DP), [58,59] gaussian approximation potential (GAP),[60] spectral neighbor analysis potential (SNAP), [61] and moment tensor potential (MTP) [45] have been reported. Among the machine learning potentials, we selected MTP because it is known as the most reasonable method in terms of performance and cost. [47] In addition, the MTPs have been successfully applied to variety of systems, such as crystal structure prediciton, [62, 63] grain boundary, [64,65] alloy, [46,66] and interface [67] research. In the MTP training, we performed hyperparameter optimization as shown in Figure S2, where the lev_{max} has a significantly effect on the accuracy compared to R_{cut} . In terms of accuracy, the best choice would be $R_{cut} = 6 \text{ \AA}$ and $lev_{max} = 16$. However, calculations using these hyperparameter settings requires around 10 times more computing times compared to hyperparameters of $R_{cut} = 5 \text{ \AA}$ and $lev_{max} = 8$. So, in terms of cost-effectiveness, hyperparameters of $R_{cut} = 5 \text{ \AA}$ and $lev_{max} = 8$ can provide effective computation time and sufficient accuracy for energy and force less with mean absolute error (MAE) less than 3 meV/atom and 0.1 meV/ \AA , respectively. Therefore, we used hyperparameters R_{cut} of 5 \AA , lev_{max} of 8, the weights of energy and force of 100:1, and a 9:1 of training sets to validation sets.[37,68] Based on these hyperparameters, the MTP was fitted to the energy and force of training sets calculated by DFT in step (4). After MTP training, we confirmed that the mean absolute errors (MAEs) of energy and force were less than 10 meV/atom and 0.02 eV/ \AA , respectively, as illustrated in Figure S3. The MTP developed in a given composition can be equally applied to any configurations of the same composition. Details of the MTP are described in Supplementary information.

2.6. MD simulation and evaluation of ionic conductivity using MTP

We sequentially performed NVT and NPT simulations on a model in which the cell size was increased to a $3 \times 3 \times 3$ supercell using the generated MTP. Due to the low ionic conductivity of SSE, the ionic

conductivities at 300 K (σ_{RT}) were obtained by extrapolating from the values for high temperatures using Arrhenius fitting. For the accurate σ_{RT} evaluation, we performed MD simulations at 7 different temperatures from 350 K to 500 K at 25 K intervals and repeated this process twice to generate an ensemble average. The target temperature was obtained by increasing the temperature by 10 K to the target temperature during 100 ps of NVT simulation. After that, the NPT simulation was carried out at a target temperature over 10 ns. Subsequently, the diffusivity was obtained from the mean square displacement (MSD) of twice-repeated NPT simulations, and the σ_{RT} was calculated using the Nernst-Einstein relation and Arrhenius fitted diffusivity at each temperature. Details of the procedure to obtain σ_{RT} are described in Supplementary information.

3. Results and discussion

3.1. Comparison and validation of developed MTPs

The halogenated Li-argyrodite ($\text{Li}_6\text{PS}_5\text{X}$ [$\text{X} = \text{Cl}, \text{Br}, \text{I}$]) structures exhibit distinctive features depending on the site occupancy of halogen at 4a and 4c sites, (i.e., site disorder), as shown in Figure S1, in which the six characteristic configurations of halogenated Li-argyrodite can be seen. [69] In ordered configurations with 0% and 100% 4c site occupancy of halogen, halogenated Li-argyrodite has very low ionic conductivity, whereas 4c site-disordered configurations with halogen ratios of 25%, 50%, and 75% show higher ionic conductivity at room temperature. [36] To verify the accuracy of the developed MTP from the PBE, PBE-D3(BJ), and optB88-vdw functionals, we determined whether the σ_{RT} of $\text{Li}_6\text{PS}_5\text{Cl}$ calculated with MTPs could represent the dependence on the site disorder. If a well-developed MTP is used for an MD simulation, it is expected to potentially overcome the disadvantages of existing AIMD, such as a relatively small cell size, high temperature and short time simulation, and high computational costs.

Table 1 shows the σ_{RT} of characteristic six configurations of $\text{Li}_6\text{PS}_5\text{Cl}$ calculated with MTPs developed from the PBE, PBE-D3(BJ), and optB88-vdw functionals compared with the value calculated by AIMD-PBE.

Table 1

Relative stability (E_{rel} , in meV per atom), Li-ion diffusion energy barrier (E_a , in meV), and Li-ion conductivity at 300 K according to site disorder, and corrected bulk Li-ion conductivity, $\sigma_{\text{bulk}}^{80\%}$, of $\text{Li}_6\text{PS}_5\text{Cl}$ calculated from AIMD_PBE, MTP_PBE, MTP_PBE-D3(BJ) and MTP_optB88-vdw.

Method	Site occupancy ($X^- @ 4c$)	E_{rel} (meV/atom)	E_a (meV)	σ_{RT} (mS/cm)
AIMD_PBE	0% ($F\bar{4}3m$)	23	452	0.0033
	25% ($R3m$)	4	193	9.1
	50% (P_2122)	0	160	23.3
	50% ($P2mm$)	11	151	37.1
	75% ($R3m$)	13	184	12.1
	100% ($F\bar{4}3m$)	206	339	0.12
	$\sigma_{\text{bulk}}^{80\%}$: 3.82			
MTP_PBE	0% ($F\bar{4}3m$)	23	529	0.007
	25% ($R3m$)	4	219	25.1
	50% (P_2122)	0	217	34.2
	50% ($P2mm$)	11	209	41.9
	75% ($R3m$)	13	239	23.4
	100% ($F\bar{4}3m$)	206	249	3.7
	$\sigma_{\text{bulk}}^{80\%}$: 4.19			
MTP_PBE-D3(BJ)	0% ($F\bar{4}3m$)	23	997	Too low
	25% ($R3m$)	4	286	3.6
	50% (P_2122)	0	290	2.7
	50% ($P2mm$)	11	290	4.4
	75% ($R3m$)	13	337	1.9
	100% ($F\bar{4}3m$)	206	271	3.7
	$\sigma_{\text{bulk}}^{80\%}$: 0.55			
MTP_optB88-vdw	0% ($F\bar{4}3m$)	23	502	0.008
	25% ($R3m$)	4	220	19.2
	50% (P_2122)	0	256	12.7
	50% ($P2mm$)	11	246	15.7
	75% ($R3m$)	13	250	13.3
	100% ($F\bar{4}3m$)	206	406	0.01
	$\sigma_{\text{bulk}}^{80\%}$: 2.46			
	$\sigma_{\text{Exp.}}$: 2.3–2.5 mS/cm			

Corrected bulk ionic conductivity, $\sigma_{\text{bulk}}^{80\%}$, was provided by considering the thermodynamic and kinetic contributions of the six characteristic configurations and 80% crystallinity of the synthesized halogenated Li-argyrodite. Details of the procedure to obtain $\sigma_{80\%}$ are described in [Supplementary information](#). In general, the $\sigma_{\text{bulk}}^{80\%}$ of AIMD and MTP calculations give overestimated values compared to with the experimental measurement of 2.3–2.5 mS/cm [15,70], except MTP_PBE-D3(BJ). And it is seen that MTP_PBE and MTP_PBE-D3(BJ) cannot correctly represent the dependence on the site disorder, where the ordered configurations with 100% 4c site occupancy of halogen exhibit an anomalously high σ_{RT} . However, MTP_optB88-vdw give very accurate $\sigma_{\text{bulk}}^{80\%}$ in close agreement with experimental values and correctly represents the site-disorder dependence as shown in the Arrhenius plots of diffusivities in [Fig. 2](#). We also verified the accuracy of MTP_optB88-vdw for $\text{Li}_6\text{PS}_5\text{Br}$ and $\text{Li}_6\text{PS}_5\text{I}$, as shown in [Table S1](#), and [Figure S5](#). Therefore, we can assert that the MTP_optB88-vdw is highly acceptable for the halogenated Li-argyrodite systems by correctly representing the structural features and potential energies in coordinate space. [37]

3.2. Large-scale and long-time MD simulations of random structures using MTP

As a promising SSE, Li-argyrodite has been reported in many studies to improve ionic conduction and thermodynamic/electrochemical stability through mixed compositions using cation mixing, halogen ratio control, and also various metal substitutions. [20–24,27,28,71–75] However, in computational simulations based on crystal structure modeling, we cannot avoid consideration of site disorder in halogenated Li-argyrodite mentioned above. Therefore, it is necessary to simulate and analyze all possible site-disorder configurations in a given composition and to perform statistical processing. In particular, $\sigma_{\text{bulk}}^{80\%}$ calculations require the σ_{RT} of six configurations and additional correction

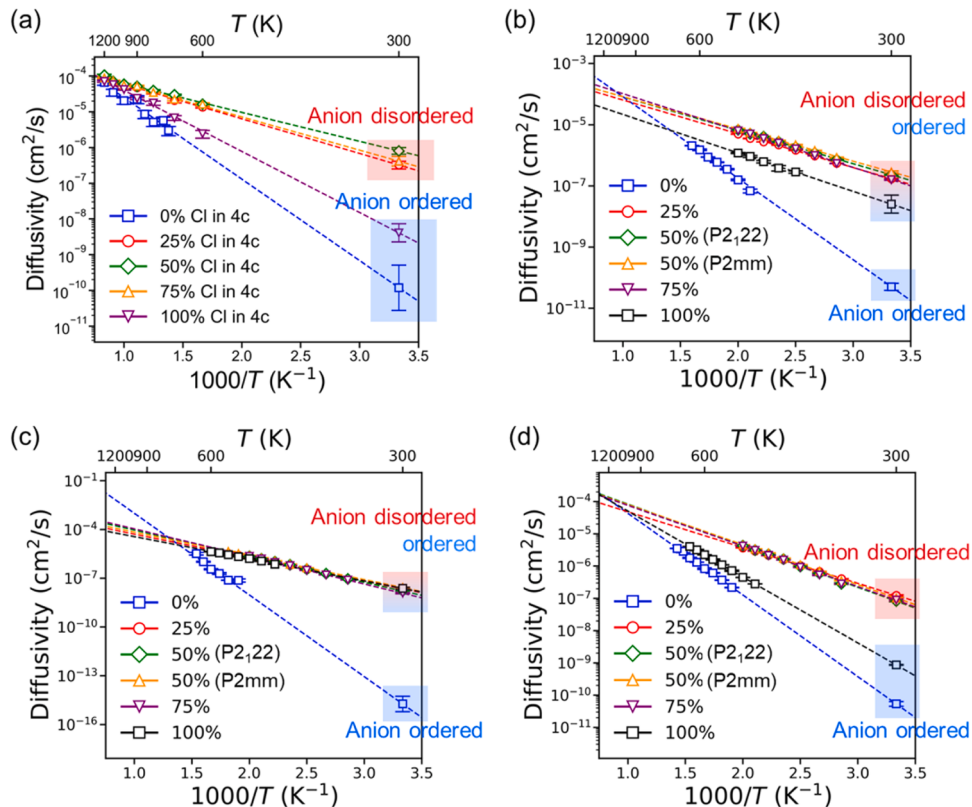


Fig. 2. Arrhenius plots of diffusivities calculated by (a) AIMD_PBE, (b) MTP_PBE, (c) MTP_PBE-D3(BJ), and (d) MTP_optB88-vdw of the six characteristic configurations of $\text{Li}_6\text{PS}_5\text{Cl}$ at temperatures range from 350 K to 700 K (from 600 K to 1200 K for AIMD_PBE) for extrapolated diffusivity at 300 K.

process, as described in [Supplementary information](#). This method is a time-consuming process and requires considerable computational resources if we use AIMD simulation. However, an MTP overcomes all these disadvantages and even enables large-scale and long-time MD simulations. Here, we designed a $3 \times 3 \times 3$ supercell structure (>1000 s atoms) with randomly arranged six types of site-disorder configurations as a representative structure that includes all configurations of argyrodite.

[Fig. 3\(a\)](#) is a schematic of a $3 \times 3 \times 3$ supercell structure composed of 27 unit-cells, considering the thermodynamic stability of the six characteristic configurations evaluated by DFT. The contributions of each configuration to the supercell structure of $\text{Li}_6\text{PS}_5\text{X}$ ($\text{X} = \text{Cl}, \text{Br}, \text{I}$) based on thermodynamic stability are described in [Table S2](#). We labeled the new supercell structure a “random structure” because the site-ordered and -disordered structures are randomly arranged. Then, we performed large-scale (>1000 s atoms) and long-time (>10 ns) MD simulations on $\text{Li}_6\text{PS}_5\text{X}$ ($\text{X}=\text{Cl}, \text{Br}, \text{I}$) random structures using MTP_optB88-vdw. [Fig. 3\(b\)](#) compares the diffusivity of the $\text{Li}_6\text{PS}_5\text{Cl}$ random structure, and the fully ordered and disordered configurations calculated in [Fig. 2\(d\)](#), in which the extrapolated diffusivity at 300 K is located between the ordered and disordered values and is close to disordered. The result implies that the random structure clearly represents the structural property of ordered and disordered structures as intended. In addition, [Table 2](#) shows the corrected bulk Li-ion conductivities ($\sigma_{\text{bulk}}^{80\%}$) of $\text{Li}_6\text{PS}_5\text{X}$ ($\text{X} = \text{Cl}, \text{Br}, \text{I}$) random structures calculated from MTP_optB88-vdw are similar to the [Table 1](#) and [Table S1](#), even experimental values. Although $\text{Li}_6\text{PS}_5\text{I}$ show relatively higher $\sigma_{\text{bulk}}^{80\%}$ of 0.5 mS/cm, it can be understood as a contribution of disordered configuration to random structure. And considering the preference of $\text{Li}_6\text{PS}_5\text{I}$ to fully ordered configuration unlike other $\text{Li}_6\text{PS}_5\text{X}$, $\sigma_{\text{bulk}}^{80\%}$ of 0.001 mS/cm for the fully ordered configuration in [Table S1](#) is much closer to the experimental value of 0.002 mS/cm.

Then, we analyzed Li-ion diffusion trajectories during MD simulations of random structures and fully ordered and disordered configurations, as shown in [Fig. 3\(c\)](#). The trajectory of the ordered configuration shows cage-like behavior without an inter-cage connection, which is evidence of low ionic conductivity. On the other hand, Li-ion diffusion is facilitated by well-formed inter-cage connections in a disordered

Table 2

Corrected bulk Li-ion conductivity of $\text{Li}_6\text{PS}_5\text{X}$ ($\text{X} = \text{Cl}, \text{Br}, \text{I}$) random structures calculated from MTP_optB88-vdw with experimental values. [15,70,76].

Composition	$\sigma_{\text{bulk}}^{100\%}$ (mS/cm)	$\sigma_{\text{bulk}}^{80\%}$ (mS/cm)	$\sigma_{\text{Exp.}}$ (mS/cm)
$\text{Li}_6\text{PS}_5\text{Cl}$	11.5	2.3	2.3 – 2.5
$\text{Li}_6\text{PS}_5\text{Br}$	8.8	1.8	1.0
$\text{Li}_6\text{PS}_5\text{I}$	2.6	0.5	0.004

configuration and can also be seen in the random structure. When we performed the same the trajectory analysis on $\text{Li}_6\text{PS}_5\text{Br}$ and $\text{Li}_6\text{PS}_5\text{I}$ ([Figure S6](#)), the Li-ion diffusion trajectories also showed the same dependence on the site disorder. In particular, $\text{Li}_6\text{PS}_5\text{I}$ create more localized Li-ion diffusion feature rather than $\text{Li}_6\text{PS}_5\text{Cl}$ and $\text{Li}_6\text{PS}_5\text{Br}$ leading to lower ionic conductivity. This trend is consistent with the previous studies of AIMD [35,36,77] and again confirms that MTP_optB88-vdw is suitable for argyrodite systems. Consequently, we found that a random structure can sufficiently represent the various configurations of argyrodite, and we therefore expect that the argyrodite-based SSE studies can be performed alone with random structures without considering all configurations, and $\sigma_{\text{bulk}}^{80\%}$ can be obtained rapidly and easily.

In this work, we verified our developed MTPs by revealing the site-disorder dependence on the Li-ion conductivity and showing the inter-cage diffusion in a random structure that enhances the Li-ion conductivity. However, although we focused on the inter-cage diffusion as a descriptor for Li-ion conductivity as reported previously, [77–79] one report noted that the rotational motion of the polyhedron increases the ionic conductivity. [43] Based on the developed MTPs, we therefore attempted to analyze the effect of PS_4 polyhedral dynamics on ionic conductivity, that is, whether the rotational motion of PS_4 polyhedron contributes to the high ionic conductivity observed in the argyrodite. We performed large-scale and long-time MD simulations of $3 \times 3 \times 3$ supercell structures at 600 K using MTP_optB88-vdw and analyzed sulfur trajectories to track the motion of PS_4 polyhedrons ([Figure S7](#)). Our results show that there is rotational motion of PS_4 polyhedron, and a vibrational motion due to the thermal effect can also be observed. To determine the effect of the vibrational motion on ionic conductivity, we compared the Li-ion diffusivity by fixing the motion of the PS_4

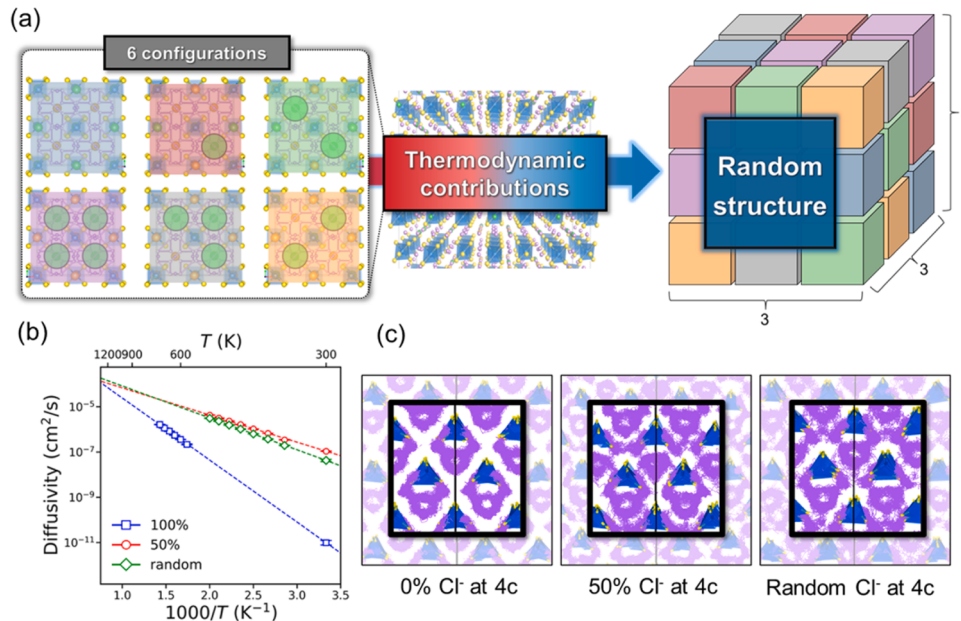


Fig. 3. (a) Schematic of a $3 \times 3 \times 3$ supercell structure composed of 27 unit-cells considering the thermodynamic stability of the six characteristic configurations. (b) An Arrhenius plot comparing the diffusivity of $\text{Li}_6\text{PS}_5\text{Cl}$ random structure and fully ordered (0% Cl^- at 4c) and disordered (50% Cl^- at 4c) configurations. (c) Li-ion diffusion trajectories during MD simulations of random structure and fully ordered and disordered configurations.

polyhedrons during MD simulations. The results in [Figure S8](#) show that the constrained motion of PS_4 polyhedrons retarded Li-ion diffusivity, however the main effect on the ionic conductivity is inter-cage diffusion, which depends on the site-disorder configuration. Although a disordered configuration is more sensitive to the constraints of PS_4 motion compared with an ordered configuration with 50% and 18% reductions, respectively, disordered configurations retain more than twice higher Li-ion diffusivity. These validations of large-scale and long-time simulation using MTPs show that MTP-based calculations can significantly improve computing time and cost efficiency while maintaining high accuracy and provide a practical approach to realistic large-scale simulations such as interfacial grain boundary (GB) systems that are inaccessible through *ab initio* calculations.

3.3. Li-ion conductivity at the grain boundary

As retardation of ionic conductivity caused by the GB [80] is a recognized obstacle to the application of SSEs to next-generation batteries, numerous efforts have been made to address the problems of GBs using DFT calculations. [81–83] However, because most DFT results are limited to simulating low-sigma (Σ) GB systems with small cell sizes of less than 20 Å, precise descriptions of experimental GB systems are difficult to produce. In addition, few theoretical reports are available on the suppression of Li-ion diffusion originating from the GBs of halogenated Li-argyrodite. To solve the problem of ionic conductivity in GB, we systematically modeled GB structures for MTP-based MD simulations and further developed a new MTP for GB systems. [Fig. 4](#) illustrates the workflow for developing a new MTP_{optB88-vdw} for GB systems through a sequential process of passive- and active-learning using additionally generated training sets for the surface and GB models. Passive learning process is almost similar to step (1) in [Fig. 1](#), with an exception for the MTP fitting process, which requires the inclusion of surface models as an additional training set. For rational GB generation,

various GB structures, including tilt and twist types, must be considered and their thermodynamic stability evaluated. Because the surface energy of halogenated Li-argyrodite has the order of (111) < (021) < (001) < (011), [84] we systematically investigated the thermodynamic stability of the designed GB models using the stable facets, as shown in [Figure S9](#). The results demonstrated that the tilt-type gives relatively better stability than twist-type and the tilt $\sum[100](021)$ GB model is the most thermodynamically stable compared to other models. Therefore, $\sum[100](021)$ GB is thermodynamically reasonable choice as the most likely GB structure in halogenated Li-argyrodite. Because our designated GB system is $\sum[100](021)$, the training set must contain (021) surfaces of [Figure S10](#) to properly characterize the GB systems, which facilitate MTP training by covering possible (021) surface-induced structural variations in the configurational space of GB model. To model the (021) surface, we used fully ordered (0% Cl^- at 4c) and disordered (50% Cl^- at 4c) configurations ([Fig. 3](#)), to which we applied a $\pm 5\%$ strain, and 10 ps AIMD simulations were used to generate 1200 structures for an additional training set. Subsequently, we developed an MTP through an active-learning process by supplementing an existing training set with an additional training set of (021) surfaces. MTPs trained at this stage may be suitable for accurately describing (021) surfaces but are not suitable for simulating GB systems due to the difficulty of characterizing interactions between surfaces.

To overcome this problem, we used an active-learning method. Active-learning a machine-learning algorithms that is used to efficiently select and label sample data for constructing a training dataset through an “active” training process. Active-learning selects the data point itself with the highest degree of uncertainty from unlabeled data and directly requests labeling data from the oracle. This helps reduce labeling costs and improve the performance of a model with fewer data. Active-learning is reported often in MTP research, and calculations for the GB of oxide materials has been reported recently. [65] The first step in the active-learning process is to set up a state construction for

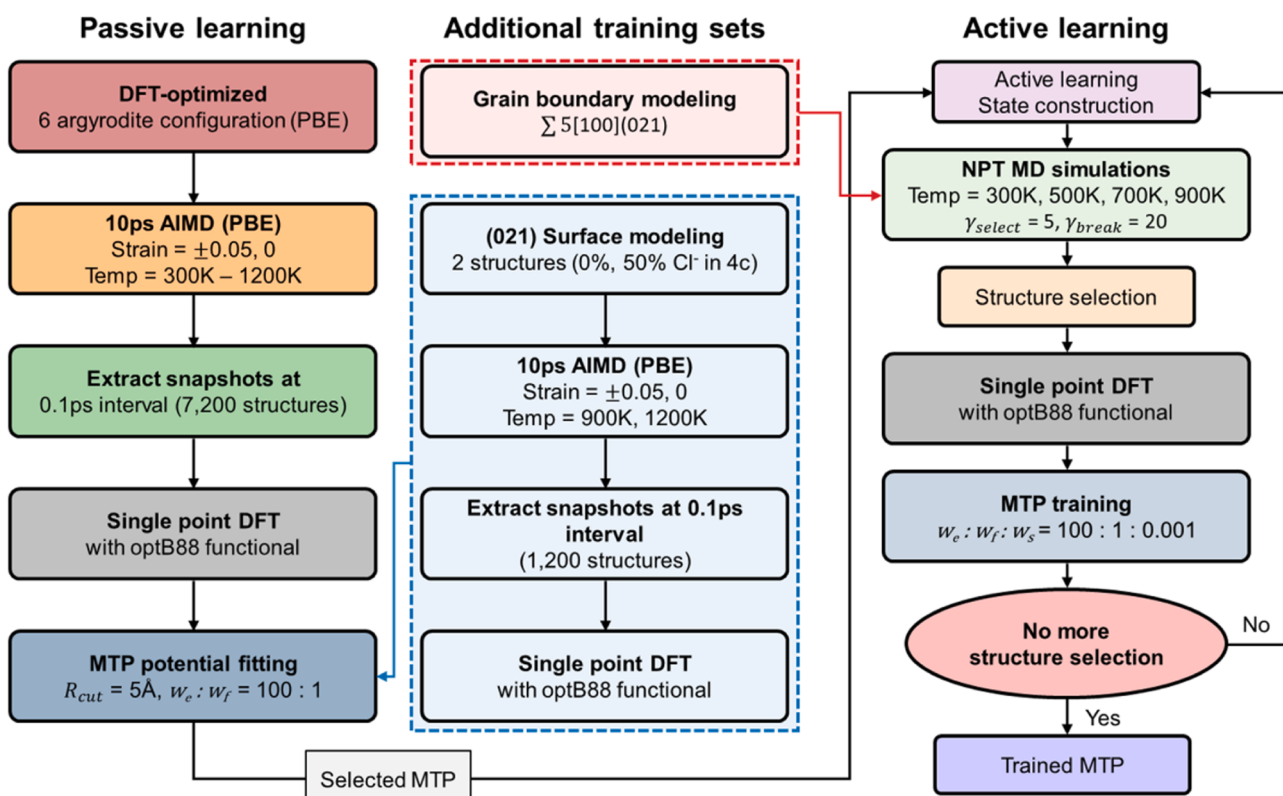


Fig. 4. (a) The workflow for developing MTPs trained at the van der Waals optB88 level of theory (MTP_{optB88-vdw}) for a GB system through a sequential process of passive and active-learning using additionally generated surface and GB models.

active-learning with MTP_optB88-vdw selected in the passive-learning process. Subsequently, NPT MD simulations are performed on the $\sum 5[100](021)$ GB model generated from each configuration of fully ordered (0% Cl⁻ at 4c) and disordered (50% Cl⁻ at 4c) Li₆PS₅Cl, as shown in Fig. 5(a), consisting of around 500 atoms using the selected MTP_optB88-vdw. (GB structure modeling is supported by GrainBoundaryGenerator module of pymatgen). In these NPT MD simulations, the dynamic structures with high uncertainties in energy, force, and stress predictions of MTP_optB88-vdw are preferentially selected for further MTP training, with fitting weights of 100:1:0.01 for energy, force, and stress, respectively. In the active-learning process, if there are no more selected structures that satisfies the criterion of $\gamma_{select}, \gamma_{break}$ to contain the various configurations in structure selection process, [46] the process is terminated and a final trained MTP is generated for GB calculations. Subsequently, we modeled $\sum 5[100](021)$ using the random structure depicted in Fig. 3(a), which considers the diverse argyrodite configurations shown in Fig. 5(b) to explore the Li-ion behavior around the GB interface. The $\sum 5[100](021)$ GB model consists of > 13,860 atoms and has lattice parameters of $a = 30 \text{ \AA}$, $b = 68 \text{ \AA}$, and $c = 135 \text{ \AA}$. Using this GB model structure and the MTP_optB88-vdw for GB, we performed a 10 ns NPT simulation at 350 K to investigate the effect of the GB region on Li-ion diffusion. The Li-ion diffusivity in the obtained from GB core region is $5.4 \times 10^{-8} \text{ cm}^2/\text{s}$, which is less than half of the value $1.8 \times 10^{-7} \text{ cm}^2/\text{s}$ in the bulk region, in agreement with the reported experimental observations, [85] as shown in Figure S11 (a). The Li-ion diffusivities along all directions are reduced compared with those of the bulk, as illustrated in Figure S11 (b), (c) and (d). Therefore, we are able to confirm that the MTP_optB88-vdw we developed works well on a GB system.

However, as mentioned above, the physical origin of the Li-ion diffusivity retardation due to GB has not yet been clarified. To address the challenges, we systematically analyzed Li-ion diffusivity by dividing the GB interface area into “GB”, “Near_GB”, “Far_GB” and “Bulk” regions. Each region is defined by 10 Å thickness, as shown in Fig. 5(c). To prove whether diffusion loss occurs due to the presence of a GB, Li-ion diffusion was evaluated by extracting the mean square displacement (MSD) of Li-ions in each region. Fig. 5(c) shows that the Li-ion diffusivity gradually decreases as it approaches the GB. The Near_GB region has higher Li-ion diffusivity compared to the GB region, but still shows low Li-ion diffusivity due to GB effect. However, it can be seen that Li-ion diffusivity in the Far_GB region, which is somewhat far from the GB region, converges to the bulk diffusivity ($1.8 \times 10^{-7} \text{ cm}^2/\text{s}$). We observed that GBs affect Li-ion diffusion within a range of at least 10 Å to 20 Å. Additionally, we analyzed the degree of structural deformation around the GB by monitoring the trajectory of each element to verify the possibility of ionic conductivity retardation due to structural changes, as shown in Figure S12. Although single anions of S²⁻ and Cl⁻ show relatively large movement around GB region due to inherent low coherency of GB, there is no significant structural change in Li-argyrodite framework. Moreover, the movement of Li-ions across the GB core region is significantly restricted. To elucidate the reason for the overall attenuation in Li-ion diffusivity caused by the GB, we monitored variation in Li-ion number in the “Near_GB”, “Far_GB” and “Bulk” regions during MTP-based MD simulations. As the MD simulation progressed, the relative Li-ion amount in GB region increases, as shown by the color change from red to blue in Fig. 5(d). This means that Li-ions start from the bulk, move sequentially towards Far_GB and Near_GB, and finally reach the GB region, accumulating Li-ions. The accumulation of Li-ions in GB region has

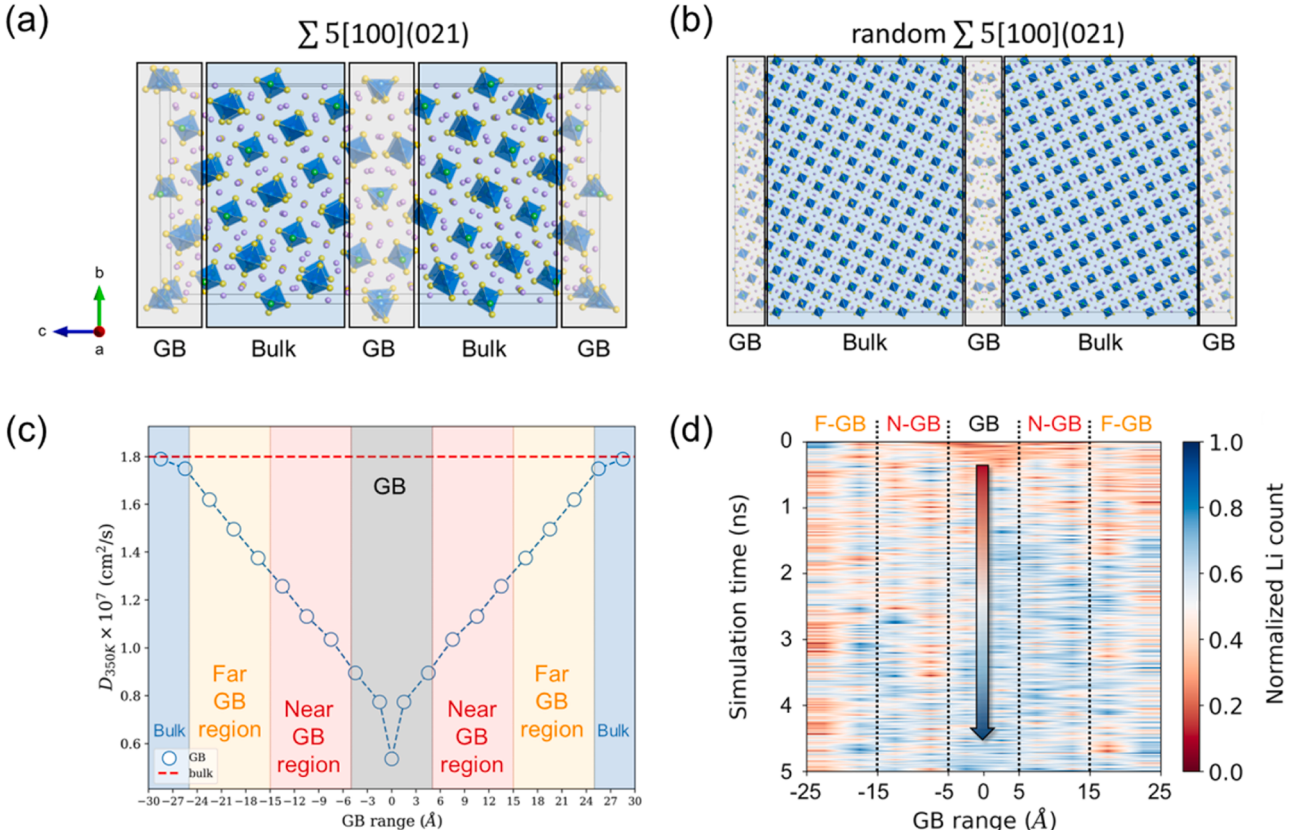


Fig. 5. $\sum 5[100](021)$ grain boundary (GB) structures generated from (a) fully ordered and disordered configurations of Li₆PS₅Cl for MTP training with lattice parameters of $a = 10.2795 \text{ \AA}$, $b = 22.9857 \text{ \AA}$, and $c = 45.9713 \text{ \AA}$ and (b) a random structure for an MTP-based MD simulation with lattice parameters of $a = 30 \text{ \AA}$, $b = 68 \text{ \AA}$, and $c = 135 \text{ \AA}$. The gray and blue shades denote the GB and Bulk region, respectively. (c) Li-ion diffusivities as a function of extent from the GB interface. The gray, red, orange, and blue regions mean “GB”, “Near_GB”, “Far_GB”, and “Bulk” regions, respectively. (d) Time evolution of normalized number of Li-ions around the GB region during 5 ns of MD simulation.

also reported due to the cation vacancies observed in the experiment. [65] And it can be expected that the degree of Li-ion accumulation correlates with a decrease in Li-ion diffusivity. Therefore, if further MD simulations are continued for a longer time, the Li-ion accumulation in the GB region will increase due to the sequential Li-ion migration, and the Li-ion diffusivity decreases further, as shown in Table S3, where 100 ps and 10 ns MD simulations produce Li-ion diffusivities of 3.4×10^{-7} cm²/s and 1.6×10^{-7} cm²/s, respectively. The accumulation of Li-ions can be analyzed by a radial distribution function (RDF) of Li-Li pairs in the GB region (Figure S13), where the RDF of Li-Li pair distance shortens significantly at 10 ns rather than at 100 ps. The reason why Li-ions accumulate in the GB is that the presence of PS₄³⁻ and S²⁻ species adjacent to each other at the GB interface generates a relatively strong negative charge around the GB region. As a result, it can be understood that electrostatic interaction becomes the driving force for the movement and accumulation of Li-ions in the GB region. Therefore, we can propose a strategy to suppress Li-ion accumulation by reducing the sulfur charge based on the solid-electrolyte inductive effect. [86] Incorporation of element with higher oxidation states weakens the S-Li interaction and eventually reduces sulfur charge due to the solid-electrolyte inductive effect. It has been reported that incorporating ions of higher oxidation states leads to improved ionic conductivity due to the solid-electrolyte inductive effect. [87] Our MTP-based large-scale and long-time simulations of $\sum 5[100](021)$ GB models successfully demonstrate the effect of the GB on the reduction of Li-ion diffusivity.

4. Conclusion

In this work, we developed machine-learned moment tensor potentials (MTPs) to overcome the limitations of *ab initio* molecular dynamics (AIMD) and systematically investigated various properties of halogenated Li-argyrodite (Li₆PS₅X [X=Cl, Br, I]). We show that the MTPs trained at the van der Waals optB88 level of theory (MTP_optB88-vdw) generate a highly reliable large-scale computational approach for realistic simulations of solid-state electrolytes (SSEs) in the bulk and at the grain boundary (GB) while maintaining predictive accuracy of ionic conductivities. The MTP-based approaches enable sufficiently large supercell structures that reflect all possible configurational disorder of experimental crystal structures as a “random structure”, provide accurate estimates of ionic conductivities close to experimentally measured values. In addition, our simulations show that not only the inter-cage diffusion but also the vibrational motion of the PS₄ polyhedron positively affects ionic conductivities. Ultimately, MTP-based large-scale and long-time MD simulations of $\sum 5[100](021)$ GB models (>10000 s atoms and > 10 ns) reveal that accumulated Li-ions around GB region induces ionic conductivity retardation and extends into an interior region of around 20 Å from the GB interface. Based on these theoretical investigations, we concluded that MTP-based simulations can significantly improve computing time and cost efficiency while maintaining high accuracy and provides a practical approach to realistic large-scale simulations, such as interfacial grain boundary (GB) systems in diverse solid-state electrolytes research fields.

CRediT authorship contribution statement

Sang Uck Lee: Supervision, Writing – review & editing, Conceptualization, Funding acquisition. **Byung-Hyun Kim:** Writing – review & editing, Software. **Yong-Gu Kim:** Resources, Writing – review & editing. **Yong Jun Jang:** Investigation, Resources, Writing – review & editing. **Byeongsun Jun:** Methodology, Software, Writing – review & editing. **Ji Hoon Kim:** Data curation, Formal analysis, Investigation, Writing – original draft. **Sun Ho Choi:** Investigation, Resources, Writing – review & editing. **Sung Man Cho:** Resources, Writing – review & editing. **Seong Hyeon Choi:** Resources, Writing – review & editing.

Declaration of Competing Interest

The authors declare that they have no known competing financial interests or personal relationships that could have appeared to influence the work reported in this paper.

Data availability

Data will be made available on request.

Acknowledgements

This research was supported by grants from the Basic Science Research Program through the National Research Foundation of Korea (NRF) funded by the Ministry of Science, ICT, and Future Planning (2021R1A2B5B01002879), the Ministry of Trade, Industry and Energy (MOTIE) of Korea (P0022336), and Hyundai Motor Company.

Appendix A. Supporting information

Supplementary data associated with this article can be found in the online version at doi:10.1016/j.nanoen.2024.109436.

References

- [1] J.B. Goodenough, Y. Kim, Challenges for rechargeable Li batteries, *Chem. Mater.* 22 (3) (2010) 587–603.
- [2] B. Dunn, H. Kamath, J.-M. Tarascon, Electrical energy storage for the grid: a battery of choices, *Science* 334 (6058) (2011) 928–935.
- [3] Q. Wang, P. Ping, X. Zhao, G. Chu, J. Sun, C. Chen, Thermal runaway caused fire and explosion of lithium ion battery, *J. Power Sources* 208 (2012) 210–224.
- [4] K.H. Park, Q. Bai, D.H. Kim, D.Y. Oh, Y. Zhu, Y. Mo, Y.S. Jung, Design strategies, practical considerations, and new solution processes of sulfide solid electrolytes for all-solid-state batteries, *Adv. Energy Mater.* 8 (18) (2018) 1800035.
- [5] T. Famprakis, P. Canepa, J.A. Dawson, M.S. Islam, C. Masquelier, Fundamentals of inorganic solid-state electrolytes for batteries, *Nat. Mater.* 18 (12) (2019) 1278–1291.
- [6] J.C. Bachman, S. Muy, A. Grimaud, H.-H. Chang, N. Pour, S.F. Lux, O. Paschos, F. Maglia, S. Lupert, P. Lamp, Inorganic solid-state electrolytes for lithium batteries: mechanisms and properties governing ion conduction, *Chem. Rev.* 116 (1) (2016) 140–162.
- [7] V. Thangadurai, H. Kaack, W.J. Weppner, Novel fast lithium ion conduction in garnet-type Li₅La₃M₂O₁₂ (M= Nb, Ta), *J. Am. Ceram. Soc.* 86 (3) (2003) 437–440.
- [8] Y. Deng, C. Eames, J.N. Chotard, F. Lalere, V. Seznec, S. Emge, O. Pecher, C. P. Grey, C. Masquelier, M.S. Islam, Structural and mechanistic insights into fast lithium-ion conduction in Li₄SiO₄-Li₃PO₄ solid electrolytes, *J. Am. Chem. Soc.* 137 (28) (2015) 9136–9145.
- [9] R. Murugan, V. Thangadurai, W. Weppner, Fast lithium ion conduction in garnet-type Li₇La₃Zr₂O₁₂, *Angew. Chem. Int. Ed.* 46 (41) (2007) 7778–7781.
- [10] Z. Liu, W. Fu, E.A. Payzant, X. Yu, Z. Wu, N.J. Dudney, J. Kiggans, K. Hong, A. J. Rondinone, C. Liang, Anomalous high ionic conductivity of nanoporous β-Li₃PS₄, *J. Am. Chem. Soc.* 135 (3) (2013) 975–978.
- [11] A. Hayashi, S. Hama, H. Morimoto, M. Tatsumisago, T. Minami, Preparation of Li₂S-P₂S₅ amorphous solid electrolytes by mechanical milling, *J. Am. Ceram. Soc.* 84 (2) (2001) 477–479.
- [12] T. Asano, A. Sakai, S. Ouchi, M. Sakaida, A. Miyazaki, S. Hasegawa, Solid halide electrolytes with high lithium-ion conductivity for application in 4 V class bulk-type all-solid-state batteries, *Adv. Mater.* 30 (44) (2018) 1803075.
- [13] X. Li, J. Liang, J. Luo, M.N. Banis, C. Wang, W. Li, S. Deng, C. Yu, F. Zhao, Y. Hu, Air-stable Li₃InCl₆ electrolyte with high voltage compatibility for all-solid-state batteries, *Energy Environ. Sci.* 12 (9) (2019) 2665–2671.
- [14] N. Kamaya, K. Homma, Y. Yamakawa, M. Hirayama, R. Kanno, M. Yonemura, T. Kamiyama, Y. Kato, S. Hama, K. Kawamoto, A lithium superionic conductor, *Nat. Mater.* 10 (9) (2011) 682–686.
- [15] P. Adeli, J.D. Bazak, K.H. Park, I. Kochetkov, A. Huq, G.R. Goward, L.F. Nazar, Boosting solid-state diffusivity and conductivity in lithium superionic argyrodites by halide substitution, *Angew. Chem. Int. Ed.* 58 (26) (2019) 8681–8686.
- [16] A. Gautam, M. Sadowski, M. Ghidlu, N. Minafra, A. Senyshyn, K. Albe, W.G. Zeier, Engineering the site-disorder and lithium distribution in the lithium superionic argyrodite Li₆PS₅Br, *Adv. Energy Mater.* 11 (5) (2021) 2003369.
- [17] C. Yu, S. Ganapathy, J. Hageman, L. Van Eijck, E.R. Van Eck, L. Zhang, T. Schwietert, S. Basak, E.M. Kelder, M. Wagelmaker, Facile synthesis toward the optimal structure-conductivity characteristics of the argyrodite Li₆PS₅Cl solid-state electrolyte, *ACS Appl. Mater. Interfaces* 10 (39) (2018) 33296–33306.
- [18] S. Yubuchi, M. Uematsu, C. Hotchama, A. Sakuda, A. Hayashi, M. Tatsumisago, An argyrodite sulfide-based superionic conductor synthesized by a liquid-phase

- technique with tetrahydrofuran and ethanol, *J. Mater. Chem. A* 7 (2) (2019) 558–566.
- [19] L. Zhou, K.-H. Park, X. Sun, F. Lalère, T. Adermann, P. Hartmann, L.F. Nazar, Solvent-engineered design of argyrodite $\text{Li}_6\text{PS}_5\text{X}$ ($\text{X} = \text{Cl}, \text{Br}, \text{I}$) solid electrolytes with high ionic conductivity, *ACS Energy Lett.* 4 (1) (2018) 265–270.
- [20] Y. Lee, J. Jeong, H.J. Lee, M. Kim, D. Han, H. Kim, J.M. Yuk, K.-W. Nam, K. Y. Chung, H.-G. Jung, Lithium argyrodite sulfide electrolytes with high ionic conductivity and air stability for all-solid-state li-ion batteries, *ACS Energy Lett.* 7 (1) (2021) 171–179.
- [21] Y. Lee, J. Jeong, H.-D. Lim, S.-O. Kim, H.-G. Jung, K.Y. Chung, S. Yu, Superionic Si-Substituted Lithium Argyrodite Sulfide Electrolyte $\text{Li}_{6+x}\text{Sb}_{1-x}\text{Si}_x\text{S}_5\text{I}$ for All-Solid-State Batteries, *ACS Sustain. Chem. Eng.* 9 (1) (2020) 120–128.
- [22] S. Ohno, B. Helm, T. Fuchs, G. Dewald, M.A. Kraft, S.P. Culver, A. Senyshyn, W. G. Zeier, Further evidence for energy landscape flattening in the superionic argyrodites $\text{Li}_{6+x}\text{P}_{1-x}\text{M}_x\text{S}_5\text{I}$ ($\text{M} = \text{Si}, \text{Ge}, \text{Sn}$), *Chem. Mater.* 31 (13) (2019) 4936–4944.
- [23] Z. Zhang, J. Zhang, H. Jia, L. Peng, T. An, J. Xie, Enhancing ionic conductivity of solid electrolyte by lithium substitution in halogenated Li-Arnyrodite, *J. Power Sources* 450 (2020) 227601.
- [24] M.A. Kraft, S. Ohno, T. Zinkevich, R. Koever, S.P. Culver, T. Fuchs, A. Senyshyn, S. Indris, B.J. Morgan, W.G. Zeier, Inducing high ionic conductivity in the lithium superionic argyrodites $\text{Li}_{6+x}\text{P}_{1-x}\text{Ge}_x\text{S}_5\text{I}$ for all-solid-state batteries, *J. Am. Chem. Soc.* 140 (47) (2018) 16330–16339.
- [25] Y.B. Song, D.H. Kim, H. Kwak, D. Han, S. Kang, J.H. Lee, S.-M. Bak, K.-W. Nam, H.-W. Lee, Y.S. Jung, Tailoring Solution-Processable Li Arnyrodites $\text{Li}_{6+x}\text{P}_{1-x}\text{M}_x\text{S}_5\text{I}$ ($\text{M} = \text{Ge}, \text{Sn}$) and their microstructural evolution revealed by Cryo-TEM for all-solid-state batteries, *Nano Lett.* 20 (6) (2020) 4337–4345.
- [26] H. Wang, C. Yu, S. Ganapathy, E.R. van Eck, L. van Eijck, M. Wagemaker, A lithium argyrodite $\text{Li}_6\text{PS}_5\text{Cl}_0.5\text{Br}_0.5$ electrolyte with improved bulk and interfacial conductivity, *J. Power Sources* 412 (2019) 29–36.
- [27] L. Zhou, A. Assoud, Q. Zhang, X. Wu, L.F. Nazar, New family of argyrodite thioantimonate lithium superionic conductors, *J. Am. Chem. Soc.* 141 (48) (2019) 19002–19013.
- [28] P. Adeli, J.D. Bazak, A. Huq, G.R. Goward, L.F. Nazar, Influence of aliovalent cation substitution and mechanical compression on Li-ion conductivity and diffusivity in argyrodite solid electrolytes, *Chem. Mater.* 33 (1) (2020) 146–157.
- [29] X. He, Y. Zhu, A. Epstein, Y. Mo, Statistical variances of diffusional properties from ab initio molecular dynamics simulations, *npj Comput. Mater.* 4 (1) (2018) 18.
- [30] Y. Zhu, X. He, Y. Mo, First principles study on electrochemical and chemical stability of solid electrolyte-electrode interfaces in all-solid-state Li-ion batteries, *J. Mater. Chem. A* 4 (9) (2016) 3253–3266.
- [31] Z. Deng, Z. Zhu, I.-H. Chu, S.P. Ong, Data-driven first-principles methods for the study and design of alkali superionic conductors, *Chem. Mater.* 29 (1) (2017) 281–288.
- [32] Z. Xu, X. Chen, K. Liu, R. Chen, X. Zeng, H. Zhu, Influence of anion charge on Li ion diffusion in a new solid-state electrolyte, Li_3LaI_6 , *Chem. Mater.* 31 (18) (2019) 7425–7433.
- [33] J. Liang, X. Li, S. Wang, K.R. Adair, W. Li, Y. Zhao, C. Wang, Y. Hu, L. Zhang, S. Zhao, Site-occupation-tuned superionic Li $x\text{ScCl}_3+x$ halide solid electrolytes for all-solid-state batteries, *J. Am. Chem. Soc.* 142 (15) (2020) 7012–7022.
- [34] Y. Deng, C. Eames, B. Fleutot, R. David, J.-N. Chotard, E. Suard, C. Masquelier, M. S. Islam, Enhancing the lithium ion conductivity in lithium superionic conductor (LISICON) solid electrolytes through a mixed polyanion effect, *ACS Appl. Mater. Interfaces* 9 (8) (2017) 7050–7058.
- [35] B.J. Morgan, Mechanistic origin of superionic lithium diffusion in anion-disordered $\text{Li}_6\text{PS}_5\text{X}$ argyrodites, *Chem. Mater.* 33 (6) (2021) 2004–2018.
- [36] B. Jun, S.U. Lee, Designing a descriptor for the computational screening of argyrodite-based solid-state superionic conductors: uniformity of ion-cage size, *J. Mater. Chem. A* 10 (14) (2022) 7888–7895.
- [37] J. Qi, S. Banerjee, Y. Zuo, C. Chen, Z. Zhu, M.H. Chandrappa, X. Li, S.P. Ong, Bridging the gap between simulated and experimental ionic conductivities in lithium superionic conductors, *Mater. Today Phys.* 21 (2021) 100463.
- [38] G. Kresse, J. Furthmüller, Efficiency of ab-initio total energy calculations for metals and semiconductors using a plane-wave basis set, *Comput. Mater. Sci.* 6 (1) (1996) 15–50.
- [39] G. Kresse, J. Furthmüller, Efficient iterative schemes for ab initio total-energy calculations using a plane-wave basis set, *Phys. Rev. B* 54 (16) (1996) 11169.
- [40] G. Kresse, J. Hafner, Ab initio molecular dynamics for open-shell transition metals, *Phys. Rev. B* 48 (17) (1993) 13115.
- [41] G. Kresse, J. Hafner, Ab initio molecular-dynamics simulation of the liquid-metal-amorphous-semiconductor transition in germanium, *Phys. Rev. B* 49 (20) (1994) 14251.
- [42] S. Plimpton, Fast parallel algorithms for short-range molecular dynamics, *J. Comput. Phys.* 117 (1) (1995) 1–19.
- [43] E.A. Wu, S. Banerjee, H. Tang, P.M. Richardson, J.-M. Doux, J. Qi, Z. Zhu, A. Grenier, Y. Li, E. Zhao, A stable cathode-solid electrolyte composite for high-voltage, long-cycle-life solid-state sodium-ion batteries, *Nat. Commun.* 12 (1) (2021) 1–11.
- [44] S.P. Ong, W.D. Richards, A. Jain, G. Hautier, M. Kocher, S. Cholia, D. Gunter, V. L. Chevrier, K.A. Persson, G. Ceder, Python materials genomics (pymatgen): a robust, open-source python library for materials analysis, *Comput. Mater. Sci.* 68 (2013) 314–319.
- [45] A.V. Shapeev, Moment tensor potentials: a class of systematically improvable interatomic potentials, *Multiscale Model. Simul.* 14 (3) (2016) 1153–1173.
- [46] I.S. Novikov, K. Gubaev, E.V. Podryabinkin, A.V. Shapeev, The MLIP package: moment tensor potentials with MPI and active learning, *Mach. Learn.: Sci. Technol.* 2 (2) (2020) 025002.
- [47] Y. Zuo, C. Chen, X. Li, Z. Deng, Y. Chen, Jr Behler, G. Csányi, A.V. Shapeev, A. P. Thompson, M.A. Wood, Performance and cost assessment of machine learning interatomic potentials, *J. Phys. Chem. A* 124 (4) (2020) 731–745.
- [48] A. Stukowski, Visualization and analysis of atomistic simulation data with OVITO—the Open Visualization Tool, *Model. Simul. Mater. Sci. Eng.* 18 (1) (2009) 015012.
- [49] P.E. Blöchl, Projector augmented-wave method, *Phys. Rev. B* 50 (24) (1994) 17953.
- [50] G. Kresse, D. Joubert, From ultrasoft pseudopotentials to the projector augmented-wave method, *Phys. Rev. b* 59 (3) (1999) 1758.
- [51] J.P. Perdew, K. Burke, M. Ernzerhof, Generalized gradient approximation made simple, *Phys. Rev. Lett.* 77 (18) (1996) 3865.
- [52] H.J. Monkhorst, J.D. Pack, Special points for Brillouin-zone integrations, *Phys. Rev. B* 13 (12) (1976) 5188.
- [53] W.G. Hoover, Canonical dynamics: equilibrium phase-space distributions, *Phys. Rev. A* 31 (3) (1985) 1695.
- [54] N. Shuichi, Constant temperature molecular dynamics methods, *Prog. Theor. Phys. Suppl.* 103 (1991) 1–46.
- [55] S. Grimme, J. Antony, S. Ehrlich, H. Krieg, A consistent and accurate ab initio parametrization of density functional dispersion correction (DFT-D) for the 94 elements H-Pu, *J. Chem. Phys.* 132 (15) (2010) 154104.
- [56] J. Klimeš, D.R. Bowler, A. Michaelides, Chemical accuracy for the van der Waals density functional, *J. Phys.: Condens. Matter* 22 (2) (2009) 022201.
- [57] K. Lee, D. Yoo, W. Jeong, S. Han, SIMPLE-NN: an efficient package for training and executing neural-network interatomic potentials, *Comput. Phys. Commun.* 242 (2019) 95–103.
- [58] L. Zhang, J. Han, H. Wang, R. Car, E. Weinan, Deep potential molecular dynamics: a scalable model with the accuracy of quantum mechanics, *Phys. Rev. Lett.* 120 (14) (2018) 143001.
- [59] S. Wang, Y. Liu, Y. Mo, Frustration in super-ionic conductors unraveled by the density of atomistic states, *Angew. Chem.* 135 (15) (2023) e202215544.
- [60] A.P. Bartók, R. Kondor, G. Csányi, On representing chemical environments, *Phys. Rev. B* 87 (18) (2013) 184115.
- [61] A.P. Thompson, L.P. Swiler, C.R. Trott, S.M. Foiles, G.J. Tucker, Spectral neighbor analysis method for automated generation of quantum-accurate interatomic potentials, *J. Comput. Phys.* 285 (2015) 316–330.
- [62] Q. Tong, P. Gao, H. Liu, Y. Xie, J. Lv, Y. Wang, J. Zhao, Combining machine learning potential and structure prediction for accelerated materials design and discovery, *J. Phys. Chem. Lett.* 11 (20) (2020) 8710–8720.
- [63] R.U. Stelzer, Y. Ikeda, P. Srinivasan, T.S. Lehmann, B. Grabowski, R. Niewa, Li_5Sn , the Most lithium-rich binary stannide: a combined experimental and computational study, *J. Am. Chem. Soc.* 144 (16) (2022) 7096–7110.
- [64] W. Ye, H. Zheng, C. Chen, S.P. Ong, A. Universal, Machine learning model for elemental grain boundary energies, *Scr. Mater.* 218 (2022) 114803.
- [65] T. Lee, J. Qi, C.A. Gadre, H. Huyan, S.-T. Ko, Y. Zuo, C. Du, J. Li, T. Aoki, R. Wu, Atomic-scale origin of the low grain-boundary resistance in perovskite solid electrolyte $\text{Li}_0.375\text{Sr}_0.4375\text{Ta}_0.75\text{Zr}_0.2503$, *Nat. Commun.* 14 (1) (2023) 1940.
- [66] K. Gubaev, E.V. Podryabinkin, G.L. Hart, A.V. Shapeev, Accelerating high-throughput searches for new alloys with active learning of interatomic potentials, *Comput. Mater. Sci.* 156 (2019) 148–156.
- [67] M.L. Holeki Chandrappa, J. Qi, C. Chen, S. Banerjee, S.P. Ong, Thermodynamics and kinetics of the cathode-electrolyte interface in all-solid-state Li-S batteries, *J. Am. Chem. Soc.* 144 (39) (2022) 18009–18022.
- [68] C. Wang, K. Aoyagi, P. Wisesa, T. Mueller, Lithium ion conduction in cathode coating materials from on-the-fly machine learning, *Chem. Mater.* 32 (9) (2020) 3741–3752.
- [69] P.R. Rayavarapu, N. Sharma, V.K. Peterson, S. Adams, Variation in structure and Li^{+} -ion migration in argyrodite-type $\text{Li}_6\text{PS}_5\text{X}$ ($\text{X} = \text{Cl}, \text{Br}, \text{I}$) solid electrolytes, *J. Solid State Electrochem.* 16 (5) (2012) 1807–1813.
- [70] W.D. Jung, J.-S. Kim, S. Choi, S. Kim, J. Jeon, H.-G. Jung, K.Y. Chung, J.-H. Lee, B.-K. Kim, J.-H. Lee, Superionic halogen-rich Li-argyrodites using in situ nanocrystal nucleation and rapid crystal growth, *Nano Lett.* 20 (4) (2020) 2303–2309.
- [71] X. Feng, P.-H. Chien, Y. Wang, S. Patel, P. Wang, H. Liu, M. Immediato-Scuotto, Y.-Y. Hu, Enhanced ion conduction by enforcing structural disorder in Li-deficient argyrodites $\text{Li}_{6-x}\text{PS}_5-x\text{Cl}_{1+x}$, *Energy Storage Mater.* 30 (2020) 67–73.
- [72] N. Minafra, S.P. Culver, T. Krauskopf, A. Senyshyn, W.G. Zeier, Effect of Si substitution on the structural and transport properties of superionic Li-argyrodites, *J. Mater. Chem. A* 6 (2) (2018) 645–651.
- [73] H.J. Deisereth, S.T. Kong, H. Eckert, J. Vannahme, C. Reiner, T. Zaiß, M. Schlosser, $\text{Li}_6\text{PS}_5\text{X}$: a class of crystalline Li-rich solids with an unusually high Li^{+} mobility, *Angew. Chem. Int. Ed.* 47 (4) (2008) 755–758.
- [74] K. Hogrefe, N. Minafra, I. Hanghofer, A. Banik, W.G. Zeier, H.M.R. Wilkening, Opening diffusion pathways through site disorder: the interplay of local structure and ion dynamics in the solid electrolyte $\text{Li}_{6+x}\text{P}_{1-x}\text{Ge}_x\text{S}_5\text{I}$ as probed by neutron diffraction and NMR, *J. Am. Chem. Soc.* 144 (4) (2022) 1795–1812.
- [75] A. Gautam, M. Ghidiu, A.-L. Hansen, S. Ohno, W.G. Zeier, Sn substitution in the lithium superionic argyrodite $\text{Li}_6\text{PC}_6\text{S}_5\text{I}$ ($\text{Ch} = \text{S}$ and Se), *Inorg. Chem.* 60 (24) (2021) 18975–18980.
- [76] H.J. Deisereth, J. Maier, K. Weichert, V. Nickel, S.T. Kong, C. Reiner, Li_7PS_6 and $\text{Li}_6\text{PS}_5\text{X}$ ($\text{X} = \text{Cl}, \text{Br}, \text{I}$): Possible Three-dimensional Diffusion Pathways for Lithium Ions and Temperature Dependence of the Ionic Conductivity by Impedance Measurements, Wiley Online Library, 2011.

- [77] N.J. De Klerk, I. Rosoń, M. Wagemaker, Diffusion mechanism of Li argyrodite solid electrolytes for Li-ion batteries and prediction of optimized halogen doping: the effect of Li vacancies, halogens, and halogen disorder, *Chem. Mater.* 28 (21) (2016) 7955–7963.
- [78] E. Zhao, L. He, Z. Zhang, J.-M. Doux, D.H. Tan, E.A. Wu, G. Deysher, Y.-T. Chen, J. Zhao, F. Wang, New insights into Li distribution in the superionic argyrodite Li₆PS₅Cl, *Chem. Commun.* 57 (82) (2021) 10787–10790.
- [79] I. Hangofer, M. Brinek, S. Eisbacher, B. Bitschnau, M. Volck, V. Hennige, I. Hanzu, D. Rettenwander, H. Wilkening, Substitutional disorder: structure and ion dynamics of the argyrodites Li₆PS₅Cl, Li₆PS₅Br and Li₆PS₅I, *Phys. Chem. Chem. Phys.* 21 (16) (2019) 8489–8507.
- [80] W.E. Tenhaeff, E. Rangasamy, Y. Wang, A.P. Sokolov, J. Wolfenstine, J. Sakamoto, N.J. Dudney, Resolving the grain boundary and lattice impedance of hot-pressed Li₇La₃Zr₂O₁₂ garnet electrolytes, *ChemElectroChem* 1 (2) (2014) 375–378.
- [81] M. Feng, J. Pan, Y. Qi, Impact of electronic properties of grain boundaries on the solid electrolyte interphases (SEIs) in Li-ion batteries, *J. Phys. Chem. C* 125 (29) (2021) 15821–15829.
- [82] J. Cui, L. Meng, S. Jiang, K. Wang, J. Qian, X. Wang, Lithium-ion diffusion in the grain boundary of polycrystalline solid electrolyte Li_{6.75}La₃Zr_{1.5}Ta_{0.5}O₁₂ (LLZTO): a computer simulation and theoretical study, *Phys. Chem. Chem. Phys.* 24 (44) (2022) 27355–27361.
- [83] Y. Zhu, Atomistic Modeling of Solid Interfaces in All-solid-state Li-ion Batteries, University of Maryland, College Park, 2018.
- [84] J. Zhang, X. Gu, Hydrolysis mechanism of Li-argyrodite Li₆PS₅Cl in air, *Rare Met.* 42 (1) (2023) 47–55.
- [85] K. Hikima, N.H.H. Phuc, H. Tsukasaki, S. Mori, H. Muto, A. Matsuda, High ionic conductivity of multivalent cation doped Li₆PS₅Cl solid electrolytes synthesized by mechanical milling, *RSC Adv.* 10 (38) (2020) 22304–22310.
- [86] S.P. Culver, A.G. Squires, N. Minafra, C.W. Armstrong, T. Krauskopf, F. Böcher, C. Li, B.J. Morgan, W.G. Zeier, Evidence for a solid-electrolyte inductive effect in the superionic conductor Li₁₀Ge_{1-x}Sn_xP₂S₁₂, *J. Am. Chem. Soc.* 142 (50) (2020) 21210–21219.
- [87] A. Hayashi, N. Masuzawa, S. Yubuchi, F. Tsuji, C. Hotohama, A. Sakuda, M. Tatsumisago, A sodium-ion sulfide solid electrolyte with unprecedented conductivity at room temperature, *Nat. Commun.* 10 (1) (2019) 5266.